nature biomedical engineering

Article

https://doi.org/10.1038/s41551-025-01603-5

Rotational ultrasound and photoacoustic tomography of the human body

Received: 16 December 2022

Accepted: 5 December 2025

Published online: 16 January 2026

Check for updates

Yang Zhang[1,2,11], Shuai Na[1,9,11], Jonathan J. Russin[3,4,5,11], Karteekeya Sastry[1,6], Li Lin[1,10], Junfu Zheng[1], Yilin Luo[1], Xin Tong[1], Yujin An[1,7], Peng Hu[1], Konstantin Maslov[1], Tze-Woei Tan[8], Charles Y. Liu[3,4,5] ✉ & Lihong V. Wang[1,6] ✉

Imaging the human body's morphological and angiographic information is essential for diagnosing, monitoring and treating medical conditions. Here we combine the power of ultrasonography for morphological assessment of soft tissue with photoacoustic tomography (PAT) for visualizing blood vessels to enable three-dimensional (3D) panoramic imaging. Specifically, fast panoramic rotational ultrasound tomography and PAT are integrated for hybrid rotational ultrasound and photoacoustic tomography (RUS-PAT), which obtains 3D ultrasound structural and PAT angiographic images of the human body quasi-simultaneously. The rotational ultrasound tomography functionality is achieved using a single-element ultrasonic transducer for ultrasound transmission and rotating arc-shaped arrays for 3D panoramic detection. By switching the acoustic source to a light source, the system is conveniently converted to PAT mode to acquire angiographic images in the same region. Using RUS-PAT, we successfully imaged the human head, breast, hand and foot with a 10-cm-diameter field of view, submillimetre isotropic resolution and 10 s imaging time for each modality. 3D RUS-PAT is a powerful tool for high-speed, dual-contrast imaging of the human body with potential for rapid clinical translation.

Imaging techniques for visualizing the human body's morphological and angiographic information, such as magnetic resonance imaging (MRI)[1] and X-ray computed tomography (CT)[2], have paved the way for medical diagnoses and physiological studies. MRI detects signals mainly from protons found in water that makes up living tissues[1], and it is routinely used in clinical applications for structural imaging throughout the body and functional imaging of the brain. CT measures the X-ray attenuation of different tissues and bones inside the body[2], and it is used to obtain anatomical information about the human body for medical diagnoses with clear advantages to MRI in diagnosing bone disorders and acute haemorrhage. Magnetic resonance angiography can image the body's blood vessels[3]. With the use of contrast agents, CT can image the angiographic information of the human body[4]. However, MRI is generally high cost, CT involves exposure to ionizing radiation, and the contrast agents have side effects.

In addition to methods based on X-ray and magnetic fields, acoustic and optical techniques have been developed for imaging the human

[1]Caltech Optical Imaging Laboratory, Andrew and Peggy Cherng Department of Medical Engineering, California Institute of Technology, Pasadena, CA, USA. [2]School of Biomedical Engineering, Tsinghua University, Beijing, China. [3]Department of Neurological Surgery, Keck School of Medicine, University of Southern California, Los Angeles, CA, USA. [4]Neurorestoration Center, Keck School of Medicine, University of Southern California, Los Angeles, CA, USA. [5]Rancho Los Amigos National Rehabilitation Center, Downey, CA, USA. [6]Caltech Optical Imaging Laboratory, Department of Electrical Engineering, California Institute of Technology, Pasadena, CA, USA. [7]Division of Biology and Biological Engineering, California Institute of Technology, Pasadena, CA, USA. [8]Keck School of Medicine, University of Southern California, Los Angeles, CA, USA. [9]Present address: China National Biomedical Imaging Center, College of Future Technology, Peking University, Beijing, China. [10]Present address: College of Biomedical Engineering and Instrument Science, Zhejiang University, Hangzhou, China. [11]These authors contributed equally: Yang Zhang, Shuai Na, Jonathan J. Russin. ✉e-mail: cliu@usc.edu; LVW@caltech.edu

https://doi.org/10.1038/s41551-025-01603-5

body in a safe and relatively cost-effective manner. Owing to its low cost and portability, ultrasonography has been widely used in clinical applications to image the heart, breast and viscera based on acoustic impedance variations[5]. However, current clinical ultrasonography is generally based on handheld phased/linear arrays[6], which have a limited field of view (FOV)[7]. For instance, these arrays have been successfully used to scan and generate full-volume breast images[8,9]; however, the scanning of these arrays faces the challenges of non-isotropic spatial resolutions. Thus, achieving a three-dimensional (3D) panoramic FOV often requires a hemispherical array configuration and many pulsers for transmission, which is not cost-effective[10,11]. In addition to scanning a linear array and using a dense hemispherical array, several other techniques exist for 3D ultrasound imaging, including the utilization of single-element transducers[11], row–column arrays[12,13] and matrix array probes[14]. Although the use of a single ultrasound sensor with a plastic aperture mask and compressed sensing has demonstrated potential in obtaining 3D images of simple structures such as letters[11], its practical application for in vivo cases remains unexplored. Row–column arrays have been investigated for 3D anatomical and functional imaging, but their limited array elements result in increased image artefacts and compromised spatial resolutions owing to line-based focusing[12,13]. Matrix array probes offer full control in transmission and reception mode, enabling fully focused ultrasound images for applications such as brain imaging within a 1-cm-diameter FOV[14]. However, the quadratic increase in the number of array elements/channels with larger apertures poses practical challenges and is not ideal for low-cost applications. Consequently, the quest for achieving high-speed, large FOV and submillimetre isotropic resolution in 3D ultrasound imaging remains an ongoing challenge in the field.

In addition, although ultrafast Doppler ultrasound has been used to image the vasculature in the brain, breast and abdomen based on the Doppler effect[15,16], it is mainly limited to the two-dimensional (2D) images. Furthermore, the application of ultrafast ultrasound localization microscopy, which involves the use of injected microbubbles, facilitates transcranial imaging of deep vasculature in the adult human brain with microscopic resolution[17]. This technique also enables the imaging of myocardial vasculature in patients through transthoracic approaches[18]. However, it is important to note that the minimally invasive requirement for microbubble injection poses limitations on its wider application. Also, it will require a large number of 2D or 3D array elements and thousands of volumes of data to generate a 3D angiographic image, which is currently not practical for a large FOV (that is, 10 cm diameter) application. Photoacoustic tomography (PAT) is based on the photoacoustic effect and combines optical absorption contrast with the high spatial resolution of ultrasound[19]. The ability to directly visualize blood vessels and to detect changes in the haemoglobin content enables the acquisition of angiographic images and extraction of functional information[20]. Although PAT has the ability to achieve high-speed large FOV 3D angiographic images[21,22], it generally does not provide sufficient scattering-based morphological contrast. One straightforward approach to combine ultrasound and photoacoustic tomography is by utilizing the same transducer array[23,24]. For instance, incorporating a light source into an existing handheld ultrasound probe enables dual-modality photoacoustic and ultrasound imaging. However, linear array-based photoacoustic imaging often faces limitations related to the limited view angle. Another approach involves the integration of a hemispherical detector array-based PAT system with linear array-based B-mode ultrasound imaging to obtain dual-modality images[25]. However, the ultrasound images generated by this method are impacted by the presence of additional hardware components and non-isotropic spatial resolution. Overall, imaging the human body's morphological and angiographic information in a high-speed, large 3D FOV, cost-effective and safe way remains challenging.

To address this challenge, we present rotational ultrasound tomography (RUST) and its combination with PAT as hybrid rotational ultrasound and photoacoustic tomography (RUS-PAT). RUST uses a single source for ultrasound transmission and a rotating array module for detection to obtain 3D structures of the human body with a large FOV (~10 cm diameter) cost-effectively. In detail, we generate wide-field acoustic waves using a single-element ultrasonic transducer and co-axially rotate the arc-shaped detection ultrasonic transducer array to achieve 3D panoramic hemispherical ultrasonic detection. A 3D volume is obtained by a voxel-based image reconstruction algorithm that considers all the detection positions after the co-axial azimuthal scan of the detection array module. A notable advantage of RUST is that it is fully compatible with PAT. By adding light illumination to the imaging object, we have integrated RUST with PAT as a hybrid RUS-PAT system, in which PAT shares the same detection mechanism with RUST. The presented hybrid tomography offers four advantages. (1) RUST outperforms the current phased/linear array-based ultrasonography by providing 3D panoramic ultrasonic detection. (2) RUST is highly compatible with the PAT system and does not require significant hardware modification. By contrast, adding conventional ultrasound tomography to a PAT system requires adding many pulsers and switches because of PAT's detection-only front-end circuit. (3) RUS-PAT is cost-effective owing to the use of a single-element ultrasonic transducer for transmission in RUST and arc-shaped arrays for detection instead of a high-cost dense hemispherical array in either RUST or PAT mode. (4) The hybrid tomography acquires both the ultrasound structural and PAT angiographic volumes of the human body at a high speed, with a large FOV and in a safe way, which may offer the opportunity for early detection and frequent tracking of diseases, including cancer[26,27].

In this study, we have used RUS-PAT to image four disparate anatomical sites in the human body—the head, breast, hand and foot with a 10-cm-diameter FOV, submillimetre spatial resolution and 10 s imaging time for each modality. The first known 3D dual-contrast head images of a hemicraniectomy patient, presented here, reveal the boundaries of the scalp and cortical region by RUST, and the vasculature in the head by PAT. These images demonstrate the potential of RUS-PAT for the evaluation of head injuries, the diagnosis of brain disease and the study of brain function. The dual-modality breast images in healthy subjects demonstrate the capability of RUST to visualize the boundary and the internal structure of the whole breast and PAT to capture the blood vessel distribution inside the breast, which potentially benefits breast

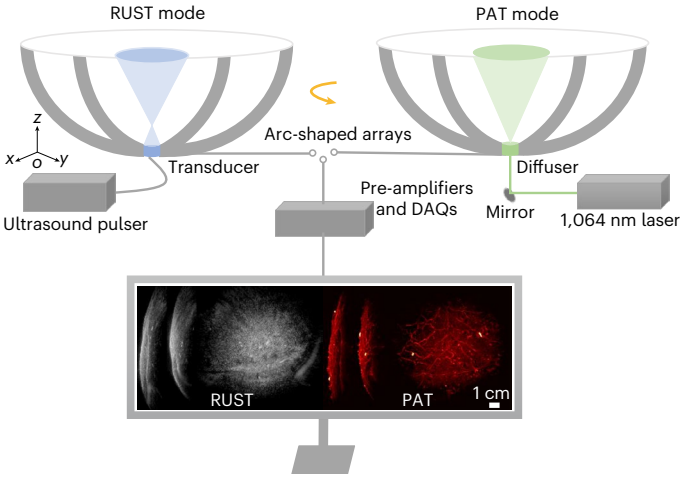

Fig. 1 | Schematic of RUS-PAT. RUS-PAT can be operated in the RUST mode and the PAT mode. In the RUST mode, a single-element ultrasonic transducer is mounted co-axially with a rotational stepper motor at the intersection of the arc-shaped detection arrays. In the PAT implementation, an engineered diffuser with a lens tube is installed at the intersection of the arc-shaped detection arrays instead of the transducer in RUST. RUST and PAT share the same detection module, which consists of arc-shaped arrays, pre-amplifiers, DAQs and a processing system.

https://doi.org/10.1038/s41551-025-01603-5

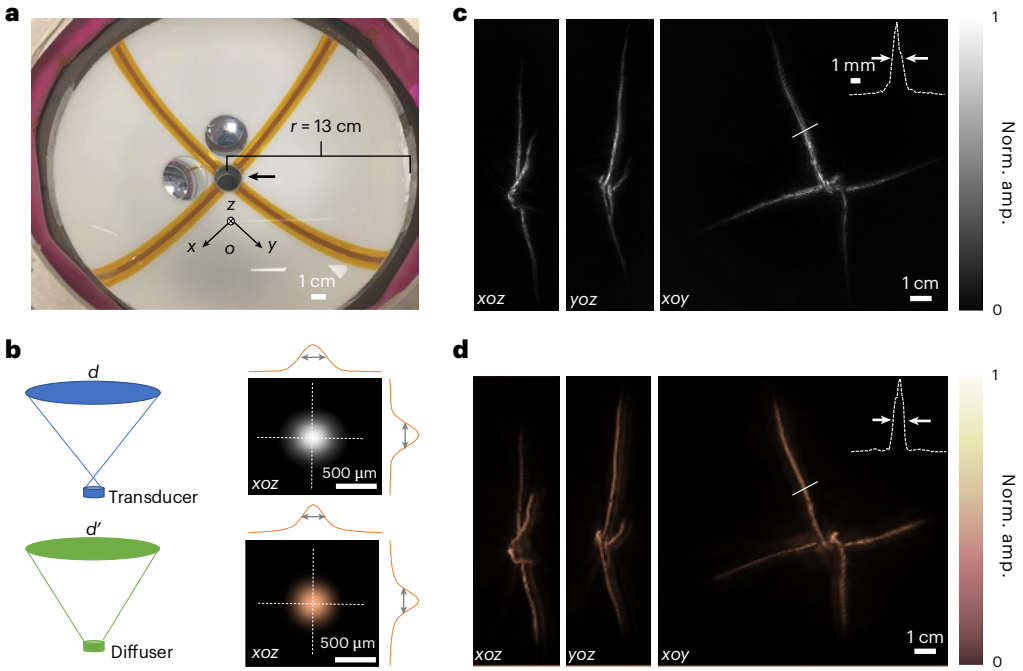

Fig. 2 | Array and phantom images. a, An example RUST set-up with four 256-element quarter-ring arrays and a single-element transducer (arrow). Note that we added two silver mirrors to help to adjust the position of the imaging target. **b**, FOV for RUST ($d \approx 10$ cm) and PAT ($d' \approx 10$ cm) set-up, and isotropic spatial resolution around 400 μm (along the x, y and z directions) for RUST (top) and PAT (bottom). **c**,**d**, A light-absorbing and ultrasound-scattering phantom was imaged using the 3D RUS-PAT system in RUST mode (**c**) and in PAT mode (**d**). The images are 12.5 cm × 12.5 cm × 3.0 cm. Norm. amp., normalized amplitude.

cancer diagnosis. The hand images show the boundaries, muscular tissue structure and blood vessel distribution in the fingers, palm and back of the hand, and exemplify the potential to play a key role in the evaluation and treatment of extremity injuries and peripheral vascular disease. The foot images demonstrate the system's ability to detect abnormalities in the foot, particularly in patients with diabetic foot ulcers. By providing detailed visualization of vascular abnormalities and tissue structures, RUS-PAT offers valuable insights into the underlying pathophysiology of diabetic foot ulcers, paving the way for more effective management strategies and personalized care for patients with diabetes.

Results

RUS-PAT implementation

In this Article, we present a fast 3D ultrasound tomography method RUST, and its combination with PAT as a hybrid RUS-PAT system to image the human body's morphological and angiographic information in a high-speed, large FOV, cost-effective and safe way. The 3D RUS-PAT system consists of four main parts, as shown in Fig. 1: (i) a single-element ultrasonic transducer with pulser for transmitting ultrasonic waves, (ii) a laser to direct light to the object, (iii) arc-shaped ultrasonic transducer arrays evenly distributed on a hemispherical bowl with an azimuthal scanning mechanism to record scattered ultrasound and photoacoustic signals panoramically, and (iv) a signal amplification, data acquisition (DAQ) and processing system, which amplifies and digitizes the signal and then reconstructs a volumetric image. The positioning of the human subjects during various imaging sessions (head, breast, hand and foot) is described in Methods and illustrated in Supplementary Fig. 1.

In the RUST implementation, we used a water-immersed 2.25 MHz single-element ultrasonic transducer as the ultrasound source. It was driven by an ultrasound pulser, which consists of a function waveform generator (20 MHz, 100 MSa s^{-1}) and a power amplifier (RF Power Amplifier, 20 kHz to 10 MHz, 50 dB) to generate a wide-field spherical wave from focus to the object (blue colour in Fig. 1). In one of the example implementations, the detection array has four 256-element quarter-ring arrays distributed on a hemispherical housing surface with a pitch of 90 degrees (centre frequency 2.25 MHz), which is azimuthally rotated using a stepper motor for panoramic detection. The number of arc-shaped arrays is flexible and can be adjusted based on the trade-off between imaging speed, scanning angular range and system cost. The source transducer was mounted co-axially with the stepper motor at the intersection of the arc-shaped detection arrays. The co-axial azimuth scanning mechanism ensures that the location of the ultrasound source does not change with the rotation of the detection arrays. With 90 degrees of continuous rotational scanning, we achieve panoramic synthetic hemispherical ultrasonic detection, which is equivalent to a physical hemispherical detection array in a cost-effective way. The detected signals are amplified and streamed to the computer through the DAQs, and they form RUST images of the human body.

The RUST system is integrated with a 3D PAT implementation[21] to achieve a hybrid RUS-PAT system. When switched to the PAT mode, an engineered diffuser within a lens tube is installed at the intersection of the arc-shaped detection arrays instead of the source transducer in RUST. We use a 1,064 nm laser with an engineered diffuser to direct a diffused light beam to the object and generate photoacoustic signals. PAT shares the same arc-shaped detection arrays, a rotational motor, DAQs and a processing system with RUST. The hybrid 3D RUS-PAT system is operated using custom software that enables dual working modes—RUST and PAT. The acquisition can start with the PAT mode, followed by the RUST mode, to obtain a dual-modality image of the human body. The DAQ and mode switching methodologies are described in Methods and in Supplementary Fig. 2. In addition, we also implemented a RUS-PAT version that can perform simultaneous RUST and PAT, as shown in Supplementary Fig. 14. In this set-up, we deliver the light from the side of the array and install a single ultrasound transducer at the bottom of the arc-shaped array. Thus, we do not need to switch the ultrasound transmission transducer and the diffuser of the light but can obtain dual image modalities of the targets without changing the imaging position. It shows comparable image features of a light-absorbing

https://doi.org/10.1038/s41551-025-01603-5

and ultrasound-scattering phantom images by PAT with bottom illumination, PAT with side illumination and RUST, respectively. The slight discrepancy between the phantom images obtained from bottom and side illumination is due to the use of different lasers, with a 20 Hz laser (Litron, pulse repetition frequency (PRF), 20 Hz; maximum pulse energy, ~2.5 J) used for bottom illumination and a 10 Hz laser (Quantel, PRF, 10 Hz; maximum pulse energy, ~850 mJ) for side illumination.

Phantom validation of RUS-PAT

We performed phantom experiments to evaluate the performance of the 3D RUS-PAT system. One example of the array set-up for RUST is shown in Fig. 2a. The single-element source transducer is at the centre (arrow) of the detection array, which has four arc-shaped arrays. The system achieved an FOV of ~10 cm and an isotropic spatial resolution of ~400 µm (along the *x*, *y* and *z* directions) for both RUST and PAT as shown in Fig. 2b. The FOV is determined by the region of the source acoustic field and the light illumination, which is smaller than the diameter of the arc-shaped arrays. The total scanning time to acquire each volumetric image is 10 s. The images of a metal wire cross phantom at a depth of 2 cm obtained using RUST and PAT are shown in Fig. 2c,d, respectively. We were able to observe comparable structures and the width of the object (~1.5 mm indicated by the profiles in Fig. 2c,d) with RUST and PAT. A comprehensive assessment of the spatial resolution uniformity for RUST and PAT across the image FOV is presented in Supplementary Figs. 3 and 4, respectively. In the case of RUST, the maximum percentage changes in spatial resolution along the *x*, *y* and *z* directions are found to be 7.8%, 5.1% and 3.5%, respectively. As for PAT, the corresponding maximum percentage changes in spatial resolution along the *x*, *y* and *z* directions are 6.4%, 5.8% and 6.3%, respectively.

To quantitatively evaluate the sensitivity distribution within the image FOV, we conducted a simulation study to assess the signal-to-noise (SNR) change, considering acoustic signal attenuation in soft tissue. The results are shown in Supplementary Fig. 5 (RUST) and Supplementary Fig. 6 (PAT). The maximal percentage change of SNR was 55% for RUST and 58% for PAT from an acoustic perspective, respectively. However, for PAT, when we considered both light and acoustic attenuation in soft tissue, the distribution of SNR in the FOV shows a drop of approximately 50 dB with a 4 cm penetration depth. In addition, we also imaged a light-absorbing and ultrasound-scattering target to experimentally evaluate the system's sensitivity and spatial resolution distribution, as shown in Supplementary Fig. 7.

RUS-PAT of the human head in vivo

Imaging the morphological and angiographic information of the head is valuable for the evaluation of head injuries[28,29], diagnosis of brain disease[30–32] and the study of brain function[14]. We imaged the skull-less hemisphere of a hemicraniectomy patient's head with RUS-PAT. The maximal amplitude projection (MAP) images of the head by 3D RUST (Fig. 3a) reveal the scalp boundary and muscular structures in the head. Images from more views of the head are also shown in Supplementary Fig. 8, and they show a clear boundary between the scalp and the cortical region of the brain (white arrows in Supplementary Fig. 8). Brain angiography images were obtained in the PAT mode (Fig. 3b), which shows the vascular network in the head. The PAT signals are related to brain function because PAT directly measures the content of haemoglobin. In addition, the patient has a surgical suture area in the head. Owing to the light-absorbing and ultrasound-scattering contrasts, we could resolve the suture area by both RUST and PAT (white arrows), and they co-registered well with each other. Overall, the 3D dual-contrast head images presented here reveal rich information for potential evaluation of head injuries, diagnosis of brain diseases and the study of brain function.

RUS-PAT of the breast in vivo

Imaging the whole-breast soft tissue and vasculature is a medical need for the monitoring and diagnosis of breast cancer[33,34]. We imaged the

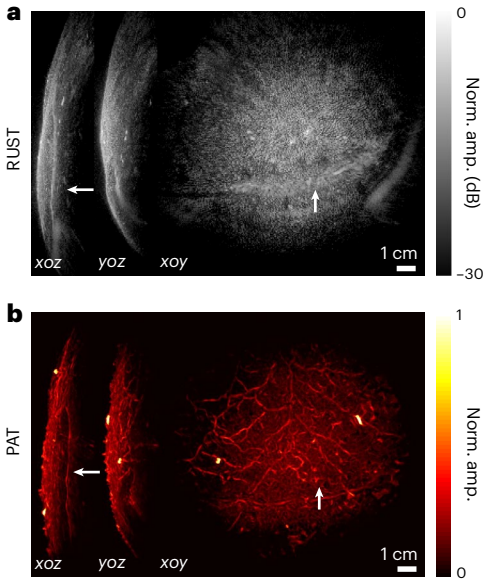

Fig. 3 | RUS-PAT images of the head. a, MAP images of the head by RUST. **b**, MAP images of the head by PAT. The images are 12.5 cm × 12.5 cm × 3.0 cm. Bright spots are the markers for PAT. The bright points in the PAT image refer to the markers on the surface of the head to assist with the co-registration of the photoacoustic images with the photograph of the head's region of interest. White arrows indicate the surgical suture area in both the RUST and PAT images.

breast of healthy subjects in a prone position using the 3D RUS-PAT system. We started with the PAT mode and acquired data within a single breath-hold of 10 s. Next, with the subject in the same position, we switched the system to the RUST mode and acquired RUST data for another 10 s. We demonstrated that RUS-PAT could provide soft-tissue ultrasound structural images (Fig. 4a,b,d,e) and PAT angiographic images (Fig. 4c,f) quasi-simultaneously. In the RUST images (Fig. 4a,b,d,e), we visualized the 3D ultrasound structures of the left and right breasts, from the skin (indicated by white arrows) to deep internal features (indicated by orange arrows). Additional MAP images and slice views of more subjects are shown in Supplementary Fig. 9c–k, providing a clear visualization of the internal structure of breast tissue from the nipple to the chest wall. In the PAT images (Fig. 4c,f), blood vessels inside the breast are well resolved. Large blood vessels are located near the skin (indicated by white arrows), and smaller blood vessels are deeper in the breast (indicated by orange arrows), which is consistent with the general angiographic anatomy of the breast. Zoomed-in side-by-side comparisons of the RUST and PAT images are shown in Supplementary Fig. 9a,b. The 3D RUST and PAT images of the breast are shown in Supplementary Videos 1–4. The dual-modality RUS-PAT images have the potential to measure the volume of the tumour using RUST and visualize the vasculature inside and close to the tumour through PAT in patients with breast cancer[35].

RUS-PAT of the extremities in vivo

Imaging the muscular tissue and vasculature of the extremities helps in evaluating injuries and screening for peripheral neurovascular diseases[36,37]. We imaged the hand palm of a healthy subject and showed the soft-tissue structure captured by RUST (Fig. 5a) and the major and minor vasculature captured by PAT (Fig. 5b), respectively. In Fig. 5b, the vessel network of the hand can be clearly tracked inside the muscular tissues. More RUS-PAT images for the whole palm, fingers and back of the hand are shown in Supplementary Fig. 10. In addition, we imaged the dorsal side of both the left and right foot of a subject. The right foot had an open wound on its dorsal side. Figure 5c,d depicts the soft-tissue structure captured by RUST and the vasculature captured by PAT of the healthy left foot, respectively. The white arrows in Fig. 5c indicate the

https://doi.org/10.1038/s41551-025-01603-5

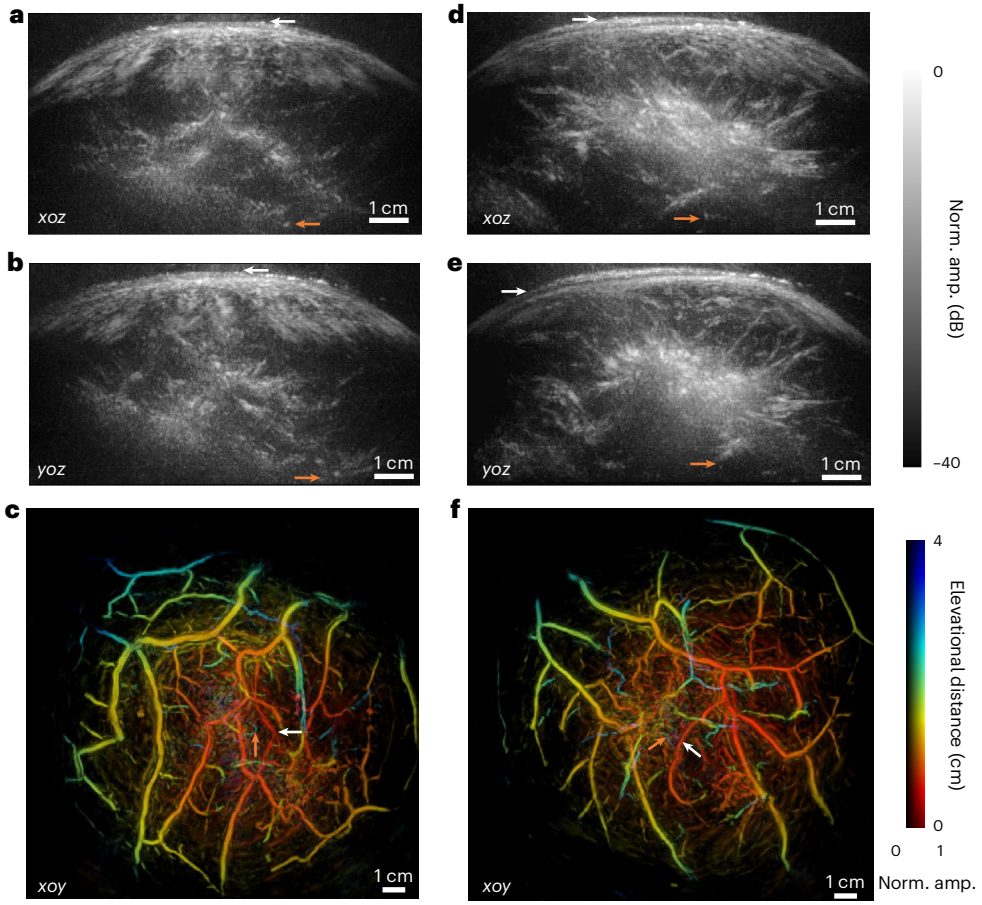

Fig. 4 | RUS-PAT images of the breast of a healthy female subject. a,**b**, MAP images of the left breast by RUST in views of *XOZ* (**a**) and *YOZ* (**b**). **c**, Elevationally encoded MAP image of the left breast by PAT. **d**,**e**, MAP images of the right breast by RUST in views of *XOZ* (**d**) and *YOZ* (**e**). **f**, Elevationally encoded MAP image of the right breast by PAT. White and orange arrows in the RUST images (**a**,**b**,**d**,**e**) indicate the skin surface and deep internal structures at a depth of approximately 5.0 cm from the skin surface, respectively. White and orange arrows in the PAT images (**c**,**f**) indicate superficial vessels close to the skin surface and deep vessels at a depth up to approximately 3.2 cm from the skin surface, respectively.

metatarsal regions of the foot. In Fig. 5e, a bright region indicated by the dashed white circle represents the wound on the dorsal side of the right foot in the RUST image. Similarly, Fig. 5f shows the wound region in the PAT image, also indicated by a white circle. Our results indicate that 3D RUS-PAT has the potential to detect tissue abnormalities by RUST and vascular abnormalities by PAT in extremities with injuries or disease.

RUS-PAT of a patient with diabetic foot in vivo

Diabetic foot ulcers are open wounds that develop on the feet of people with diabetes owing to nerve damage, poor circulation and impaired healing. Without proper care, they can lead to infections and even amputation. We imaged a patient with diabetic foot ulcers using our RUS-PAT system. Figure 6a–c depicts the photograph, the soft-tissue structure captured by RUST and the vasculature captured by PAT of the normal left foot, respectively. The right foot of the patient had an ulcer on the bottom and only four toes. In Fig. 6e,h, a bright region indicated by the square box and dashed white circle represents the foot ulcer on the bottom of the right foot in the RUST image. Similarly, Fig. 6f,i shows the foot ulcer region in the PAT image, also indicated by the square box and a white circle. In addition, we observed the loss of the thumb toe's feature in RUST (Fig. 6e) and PAT (Fig. 6f), which matches the photograph (Fig. 6d). Note that the bright spots, as indicated by the solid white arrows in Fig. 6f, correspond to the surgical suture region of the foot, and the features, as indicated by the dashed white arrows in Fig. 6e, correspond to the band tape on the surface of the toes. Our results indicate that 3D RUS-PAT has the potential to detect diabetic foot ulcers in patients.

Discussion

By imaging both morphological and angiographic information quasi-simultaneously with a large FOV (~10 cm diameter), submillimetre isotropic resolution (~400 µm) and high speed (10 s), RUS-PAT has the potential for rapid clinical translation. A major advantage of RUS-PAT for human medical imaging is that it requires neither exogenous contrast agents nor ionizing radiation, improving safety for the patient. In this study, we achieved volumetric ultrasound structural and PAT angiographic images in the human head, breast, hand and foot. For the head imaging, we imaged a hemicraniectomy patient's skull-less hemisphere because the skull presents a major obstacle for transcranial ultrasound tomography and PAT with a 2.25 MHz ultrasound centre frequency of the current system. Here the intention was to showcase the capabilities of the system in imaging brain tissue and detecting potential abnormalities or pathologies. A lower ultrasound centre frequency can be utilized for transcranial application in the future. For the breast application, we imaged healthy breasts to demonstrate the capabilities of RUS-PAT to obtain the soft-tissue structures and blood vessels inside the whole breast. Evaluation of the performance of RUS-PAT in a patient with breast cancer would be of major interest. One of the expectations is that RUST can detect the location and measure the volume of the tumour, and PAT can obtain the vasculature distribution

https://doi.org/10.1038/s41551-025-01603-5

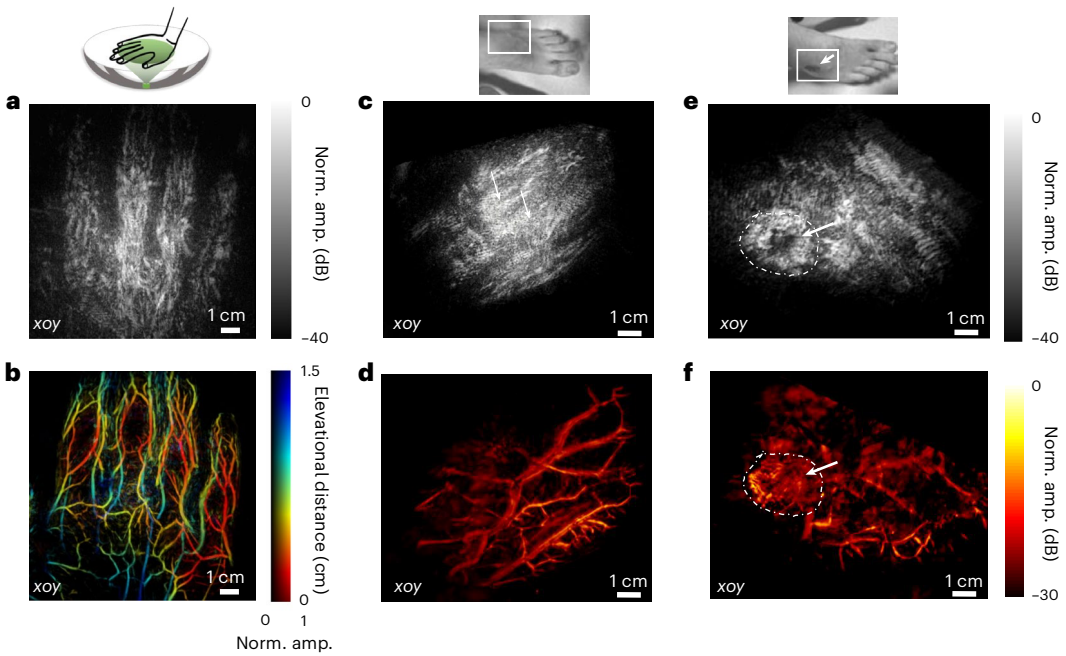

Fig. 5 | RUS-PAT images of the hand and foot. a, MAP images of the hand by RUST. **b**, MAP images of the hand by PAT. The images are 10.0 × 10.0 × 1.5 cm. **c**, MAP images of the dorsal side of the left foot by RUST. The white arrows indicate the metatarsal regions of the foot. **d**, MAP images of the dorsal side of the left foot by PAT. **e**, MAP images of the dorsal side of the injured right foot by RUST. **f**, MAP images of the dorsal side of the injured right foot by PAT. The white arrows and dashed white outlines (**e**,**f**) represent the wound on the foot. The white boxes in the photographs represent the respective regions of the feet being imaged.

of the tumour region, which will benefit the early diagnosis of breast cancer[10]. For the hand images, the morphological and angiographic information of the hand can be potentially used for biometric identification in healthy subjects[38,39]. RUS-PAT also has the potential to be used for the evaluation of hand injuries, to detect structural pathology such as a cyst in the hand, to monitor postoperative limb reconstruction/salvage outcomes and for the evaluation of peripheral vascular disease[40]. Another impactful application in the extremities might be with diabetic foot, where chronic ischaemia, wound tissues and infections make RUS-PAT a potential clinical imaging technique. We imaged a patient with diabetic foot ulcers on the bottom of the foot. Our results demonstrate that RUS-PAT can detect tissue abnormalities through RUST and vascular abnormalities through PAT in patients with diabetic foot ulcers. In addition, RUS-PAT can also be used for other parts of the human body, such as the abdomen, by adjusting the position of the system and the subject. In addition, free flaps in plastic surgery might be another application where RUS-PAT might find immediate value in the critical first few days after surgery.

Several key features make RUS-PAT a unique tool for 3D dual-contrast imaging. The rotating mechanism ensures that we can use arc-shaped arrays to synthesize a hemispherical array with a panoramic detection view for both RUST and PAT. The use of a separated single-element ultrasonic transducer for transmission in RUST ensures that it is highly compatible with the PAT system, which has a detection-only front-end circuit. The use of a single-element transmission transducer and arc-shaped detection arrays makes RUS-PAT achieve panoramic 3D imaging in a cost-effective way because it does not require a physical hemispherical array with a large number of array elements and their corresponding detection channels. The PAT mode uses the same detection module as the RUST mode, which reduces system complexity. We have developed a switch methodology (Supplementary Fig. 2) to ensure that the subject remains in the same position during the RUST and PAT modes. The system is also capable of performing RUST and PAT simultaneously by delivering light from the side of the array and installing a single ultrasound transducer at the bottom of the arc-shaped array (Supplementary Fig. 14).

The 3D RUS-PAT system is flexible with the choice of the ultrasound centre frequency, the number of arc-shaped arrays and the imaging time. In the current set-up, we used a detection array with a centre frequency of 2.25 MHz. It is possible to use a much higher transducer frequency, such as 5 MHz, for an improved spatial resolution for human breast, hand and foot imaging at the cost of reduced penetration depth. Similarly, we can use a 1 MHz centre frequency for transcranial human head imaging at the cost of reduced spatial resolution. The choice of the number of arc-shaped arrays depends on the trade-off between imaging speed, SNR and hardware cost. We can reduce the number of arcs by using a single-arc set-up but with a 360 degrees mechanical scanning angle. This set-up requires four times the scanning time but reduces the number of array elements and DAQ channels by four times compared with a four-arc set-up, thus reducing the cost further. We can also increase the number of arc-shaped arrays to 8, 16 or even more to increase the imaging speed to capture functional information and image fast phenomena in the human body with increased hardware cost. The scanning time can be reduced to 2 s when we operate a higher speed motor and use a higher pulse repetition rate (that is, 50 Hz) for ultrasound and light transmission to ensure a densely sampled hemispherical detection matrix. With such a high speed, single breath-hold imaging of different parts of the human body can be achieved with minimal motion during acquisition. Furthermore, in the current implementation, the ultrasound and light source have been installed at the bottom of the array. However, it is worth noting that we have the flexibility to adjust their positions to other locations, such as the side of the array. This alternative configuration holds the potential to serve as additional sources, thereby enhancing the SNR within the entire volume.

In this study, we have successfully developed a proof-of-concept system for imaging representative areas of the human body. Our system enables the acquisition of both morphological and angiographic information in a quasi-simultaneous manner, offering a large FOV (approximately 10 cm diameter), submillimetre isotropic resolution (around 400 μm) and high-speed imaging capabilities (10 s) for regions such as the human head, breast, hand and foot. However, it is important

to acknowledge the limitations and the direction of further improvement of our current study.

1) The sensitivity for detecting small blood vessels. We performed the analysis of the sensitivity for detecting small blood vessels in the head, breast and extremities, as shown in Supplementary Fig. 11. The measured smallest diameters of the blood vessels of the hand, breast and head in the PAT images are 0.62 ± 0.06 mm (at a depth of 1.0 mm), 0.60 ± 0.03 mm (at a depth of 1.0 cm) and 0.61 ± 0.10 mm (at a depth of 3.0 mm), respectively. Note that the in vivo blood vessels may be smaller than the measured value owing to the spatial resolution of the system. While our current system demonstrates the capability to detect submillimetre blood vessels, there is room for further improvement. To enhance the spatial resolution, we could explore the use of a wider ultrasound band, which would enable us to delineate even smaller blood vessels below 100 µm in diameter. In addition, using SNR boosting techniques such as incorporating additional sources could contribute to better imaging quality and more precise visualization of these tiny blood vessels. Thus, by using these techniques, we may achieve even greater resolution and sensitivity in our imaging system.
2) Penetration depth and volumetric coverage. In our current implementation, we have achieved a penetration depth of 5 cm with RUST imaging, as shown in Fig. 4 and Supplementary Fig. 9. For breast imaging using PAT, we have achieved a penetration depth of 3.2 cm in 1 female subject, as shown in Fig. 4. The slightly shallower penetration depth of the breast compared with a previous study[22] is due to the use of water instead of deuterium oxide (D_2O). These depths allow us to access the cortex region of the human brain, a significant portion of the breast and the entire hand. However, there is potential for further exploration to observe deeper features, particularly in deep brain imaging and whole-breast imaging to the chest wall. By pushing the depth limit (for example, the use of lower centre frequency transducer arrays and optimal laser wavelengths), we may capture more comprehensive information from these regions. Furthermore, our system offers an FOV with a diameter of 10 cm in the horizontal direction. This FOV is sufficient for capturing images of most parts of the head, breast, hand and foot. Note that this FOV can also be adjusted by changing the diverging angle of the engineering diffuser and the position of the source ultrasound transducer. Moreover, to enable whole-body imaging, particularly for the abdomen region, it is possible to enlarge the FOV by utilizing a larger diameter for the arc-shaped array. This enhancement would facilitate more comprehensive imaging coverage of the entire body.
3) System adaption for different target sizes. The transducer array used in our RUS-PAT system was designed with a 13 cm radius. This size was selected to accommodate a wide range of head sizes and breast sizes typically encountered in clinical practice. The 13 cm radius offers sufficient coverage for most individuals, allowing adequate imaging of the target area of interest. We added Supplementary Figs. 1 and 12 to illustrate the experimental set-up, in which the target was supported by the plastic film, which can support various sizes and geometries. While the fixed size of the transducer array provides versatility in accommodating various head and breast sizes, we acknowledge that there may be limitations for extremely large or small anatomical structures. Future work includes the design of more advanced holders for different sizes of head, breast and other body regions.
4) Comparison of RUST with clinical handheld ultrasound. The large 3D FOV (10 cm diameter) offered by RUST enables whole organ imaging, such as the entire breast or hand, with a single acquisition. By contrast, conventional handheld linear array probes typically provide only 2D images with limited FOV (less than 5 cm). The handheld operation of conventional probes allows clinicians to explore the region of interest through multiple trials. However, this flexibility can introduce operator-dependent imaging results and discrepancies between visits owing to variations in operations and imaging locations. By contrast, our RUST system overcomes these limitations by capturing whole-breast and hand images in a single acquisition, potentially providing more reliable and consistent results compared with handheld operations. While the current implementation of RUST is not designed for handheld use, we acknowledge the value of a handheld version. In fact, we envision the possibility of implementing the RUST concept in a handheld probe by utilizing a smaller diameter arc array and a lightweight rotational motor, accompanied by a longer electrical cable for connection to the DAQ system. This handheld version could serve as a complementary bedside application, providing clinicians with the flexibility they are accustomed to, albeit with a relatively smaller FOV. We understand that adopting new technology in a clinical setting can present challenges. However, we firmly believe that with proper training and familiarization, clinicians can effectively adapt to using RUST. The operation of RUST is similar to other existing medical imaging devices, such as CT, MRI and ultrasound systems. Therefore, clinicians can leverage their existing expertise and familiarity with these modalities to easily integrate RUST into their clinical workflow.

For the ultrasound mode of RUS-PAT, we have included results demonstrating breast imaging using our current 2.25 MHz system compared with a standard linear array probe (ATL P4-2, centre frequency 2.5 MHz), with both operating approximately at the same centre frequency. We selected the same centre frequency for the linear array probe to ensure a fair comparison, as the RUS-PAT method is adaptable to different centre frequencies. As presented in the added Supplementary Fig. 15, a standard linear array probe was used to image the same breast subject, matching the centre frequency of the RUS-PAT system. Two comparable planes were selected from the 2D slices of the 3D RUST images and the corresponding linear array images for comparison. The linear array imaging sequence was performed using standard B-mode focused ultrasound imaging. By comparing Supplementary Fig. 15c,d, as well as Supplementary Fig. 15h,i, it is evident that RUST provides significantly better spatial resolution and more precise delineation of breast structures than the standard linear array probe. The slight discrepancies between Supplementary Fig. 15c,d, as well as Supplementary Fig. 15h,i, can be attributed to gentle compression of the breast by the linear array probe and positional differences during imaging. We have also added breast images acquired using a higher centre frequency (8 MHz) linear array probe, which is commonly used in clinical settings. As expected, the higher-frequency probe provides improved B-mode image quality and clearer boundary definition. These results suggest that implementing a higher-frequency version of the RUST system could further enhance image quality. Notably, the MAP images from our current system (Supplementary Fig. 15a,f) demonstrate comparable structural features and offer volumetric anatomical context that is not accessible with standard 2D scans.

We have also added a comparison of RUS-PAT in photoacoustic mode with state-of-the-art Doppler ultrasound imaging. As shown in Supplementary Fig. 16, we acquired hand images using RUS-PAT, ultrafast Doppler ultrasound with a matrix array probe (1,024 elements, 0.3 mm pitch, 8 MHz centre frequency) and ultrafast Doppler ultrasound with a linear array probe (256 elements, 15 MHz centre frequency, LZ250). One notable advantage of RUS-PAT is its large FOV, approximately 10 cm in diameter (Supplementary Fig. 16a), compared with the matrix array's ~1 cm (Supplementary Fig. 16b) and the linear array's ~2 cm 2D slice (Supplementary Fig. 16c). The regions imaged

https://doi.org/10.1038/s41551-025-01603-5

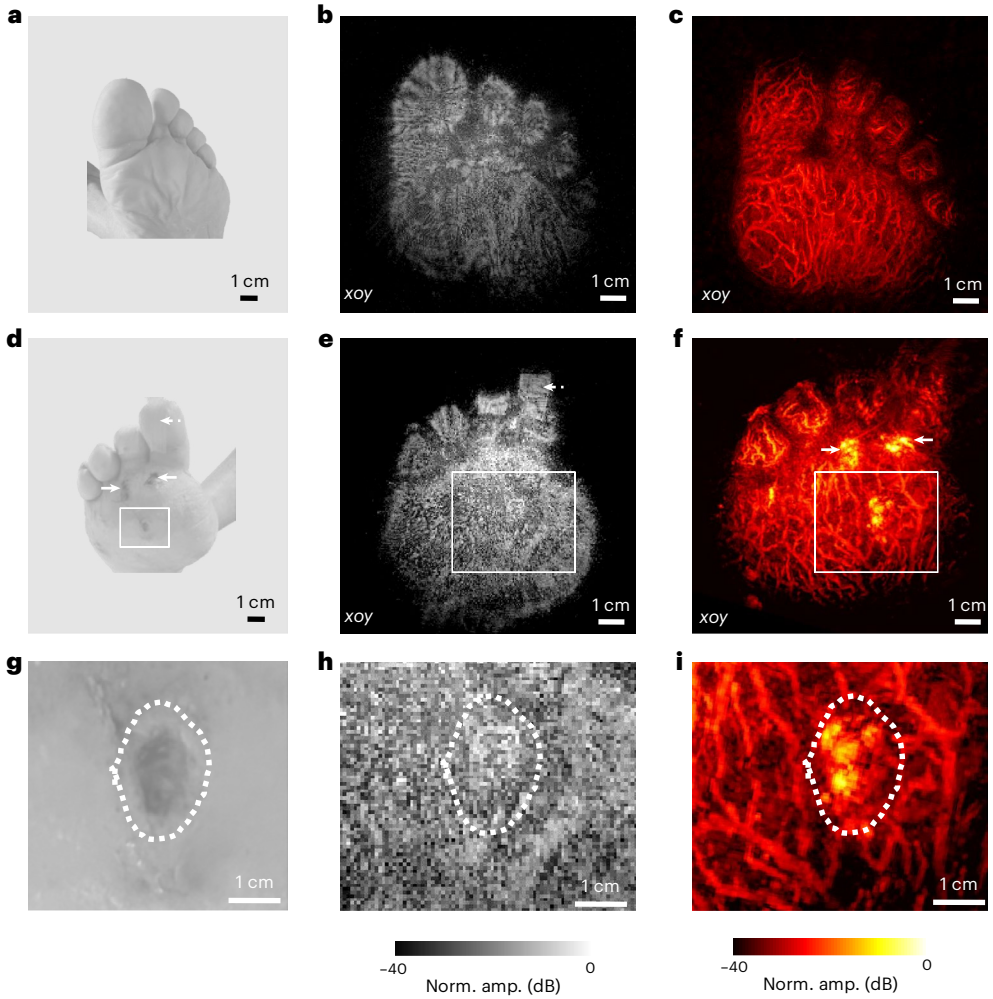

Fig. 6 | RUS-PAT images of a patient with diabetic foot ulcers. a–**c**, Photograph (**a**), MAP RUST images (**b**) and MAP PAT images (**c**) of the normal left foot. **d**–**f**, Photograph (**d**), MAP RUST images (**e**) and MAP PAT images (**f**) of the abnormal right foot. **g**–**i**, Zoomed-in photograph (**g**), MAP RUST images (**h**) and MAP PAT images (**i**) of the abnormal right foot.

by the matrix array and linear array Doppler ultrasound correspond to the white box and dashed green line in Supplementary Fig. 16a, respectively. The images clearly demonstrate that RUS-PAT captures the majority of the hand region and provides a detailed view of the blood vessel network. By contrast, Doppler ultrasound captures only two blood vessels with the matrix array or a single blood vessel with the linear array. Another key difference between RUS-PAT and state-of-the-art Doppler ultrasound lies in the physical meaning of the images. RUS-PAT measures relative haemoglobin content, whereas Doppler ultrasound detects blood flow. We believe that RUS-PAT can serve as a highly complementary tool to Doppler ultrasound, providing rich and complementary information about the circulatory system.

5) Image quality and artefacts. In the case of breast imaging, the dark gap observed in the image (Fig. 4a) is due to the relatively weak scattered ultrasound signals from the corresponding breast tissue. In the case of extremity imaging, we observed striation patterns on the surface of the foot in the RUST images (Fig. 6b). These patterns can be attributed to the geometric characteristics of the tissue surface (as indicated by the photograph Fig. 6a) and may also be influenced by speckle artefacts. To address this, further exploration of data processing techniques is warranted (for example, speckle reduction). These techniques could potentially help in removing or utilizing this pattern to extract additional information from the extremity images. In addition, we chose to use a 30 dB or 40 dB log compression threshold for displaying the ultrasound images, as it provides a good balance between image contrast and detail in our case. Achieving higher image contrast or dynamic range (up to 60 dB) could be possible with advanced hardware configurations (for example, higher centre frequency ultrasound arrays) or more sophisticated data processing techniques (for example, adaptive image reconstruction methods).
6) Overall cost. To analyse the overall cost of the current RUS-PAT system implementation, we need to consider the arc-shaped arrays, the pre-amplifiers, the DAQ modules, the laser and the host computer. One of the significant contributions of our work is that we have offered a cost-effective solution for adding ultrasound imaging modality to the photoacoustic CT system. In detail, the RUST concept is highly compatible with PAT because it uses a separate single-element transducer for transmission and, therefore, does not require significant hardware modification. By contrast, adding conventional ultrasonography to a photoacoustic system requires the addition of hundreds or thousands of pulsers and switches owing to PAT's detection-only front-end circuit. In addition, we have exploited the rotational mechanism with arc-shaped detection arrays to achieve 3D panoramic ultrasonic detection for both ultrasound and photoacoustic

tomography in a cost-effective way from the ultrasound array perspective, instead of using a high-cost, dense, hemispherical array. Since our current implementation does not introduce a new method for reducing the cost of the PAT component, we acknowledge that the overall system cost is largely determined by this component, which is a limitation of current PAT systems. To address this issue, future efforts may focus on leveraging low-cost light delivery (for example, LED array) and acoustic detection array technologies (for example, a single arc-shaped array, at the cost of increased imaging time).

7) Potential for future clinical application. The current study introduces an accessible and adaptable implementation of RUS-PAT that integrates 3D ultrasound tomography with PAT. While the system is in an early stage, its modular design offers flexibility for future optimization towards different clinical needs. In breast imaging, the current RUS-PAT set-up has enabled dual-modality 3D ultrasound and photoacoustic angiography images in healthy volunteers, with depth coverage sufficient to capture a substantial portion of the breast, including areas of potential clinical interest. With further system refinements—such as using higher-frequency ultrasound arrays and improved illumination strategies—there is potential to enhance image resolution and coverage for more comprehensive breast assessment. In detail, with additional modifications—such as breast compression and dual-sided illumination—full-breast PAT may become feasible. In addition, it is important to note that current clinical breast ultrasound often utilizes higher-frequency probes (8–15 MHz), whereas our prototype uses a 2.25 MHz array. Future versions may incorporate higher-frequency arrays to enhance spatial resolution, although this may limit imaging depth. In head imaging, the ability to detect cranial sutures demonstrates sensitivity to anatomical landmarks, suggesting feasibility for exploring superficial cerebral vasculature in future studies. For hand imaging, the system shows promise in visualizing structures such as blood vessels, tendons and joints, which may support future investigations into musculoskeletal and vascular conditions. In addition, initial application of the system in patients with diabetic foot ulcers indicates potential for assessing tissue damage and vascular changes. While these early demonstrations are encouraging, further validation with larger cohorts and condition-specific adaptations will be necessary to fully evaluate the system's clinical relevance across these applications.

When compared with existing ultrasound technologies, RUS-PAT provides a set of complementary features rather than a direct replacement for current systems. Although part of the resolution benefit arises from the large aperture coverage, conventional ring-array ultrasound tomography systems generally produce 2D reconstructions and require a large number of transmitting elements and driving circuits, which increases hardware complexity. By contrast, the present RUS-PAT implementation achieves volumetric 3D imaging with a single-element transducer for transmission, thereby reducing hardware demands. In addition, existing ring-array breast imaging systems are not combined with photoacoustic capability and therefore cannot provide vascular information, whereas RUS-PAT integrates both structural ultrasound tomography and photoacoustic angiography within one platform. High-frequency linear array systems are capable of great 2D imaging, particularly for superficial targets. However, reconstructing 3D datasets with such probes generally requires mechanical scanning, which introduces several limitations: elevational resolution is constrained by probe geometry, motion during scanning can affect image quality, and acquisition times may be prolonged for larger fields of view. RUS-PAT addresses some of these limitations by enabling hands-free volumetric imaging with relatively isotropic resolution across a wide region. While the B-mode image quality of the current prototype is lower than that of high-frequency clinical arrays, the combined acquisition of 3D ultrasound and photoacoustic information provides anatomical and vascular context that 2D scans may not readily achieve. The system is also compatible with photoacoustic contrasts beyond haemoglobin. Multi-wavelength excitation could allow estimation of both oxy- and deoxy-haemoglobin molecules, and other endogenous absorbers (for example, lipids and water) or exogenous probes (for example, dyes and nanoparticles) may be used to extend the method towards functional, metabolic and molecular imaging. For certain clinical applications, such as diabetic foot ulcers, high-frequency probes may be sufficient for superficial structural imaging. In this context, the additional contribution of RUS-PAT lies in volumetric assessment of tissue morphology, haemoglobin-sensitive vascular contrast for potentially evaluating perfusion and reduced operator dependence through fixed scanning geometry. Overall, RUS-PAT is not intended to replace state-of-the-art ultrasound or photoacoustic systems but to offer a complementary, dual-modality approach for volumetric imaging across multiple anatomical regions. Future iterations that incorporate higher-frequency arrays and improved illumination strategies may help to enhance resolution and extend the range of potential clinical and research applications.

In this pilot study, we demonstrated RUST's ability to achieve a large FOV anatomical image at high speed and its flexibility to be compatible with PAT as RUS-PAT for obtaining both the ultrasound structural and PAT angiographic images of the human body. This state-of-the-art dual-contrast RUS-PAT system provides volumetric imaging of the human body in a high-speed, large 3D FOV, cost-effective and safe way, which is viable for clinical translation.

Methods

3D RUST design and construction

The 3D RUST design comprises a source ultrasound transducer, an ultrasound detection module and a rotation scanner. The ultrasound source was a spherical focused single-element transducer (Olympus, focal length = 1 inch, diameter = 0.75 inch, 2.25 MHz centre frequency). The transducer generates a virtual point source in front of the transducer surface. In one of the example demonstrations, ultrasound detection was implemented by four 256-element quarter-ring ultrasonic transducer arrays evenly distributed on a hemispherical bowl (130 mm radius) with a separation of 90 degrees. The array elements are unfocused with a 0.6 mm × 0.7 mm active element size, 0.74 mm element pitch and 2.25 MHz centre frequency with a one-way 78% fractional bandwidth. The number of arc-shaped arrays used is flexible and can be adjusted to 1, 2, 4, 8 or even more. The 1,024 detection elements are directly connected to four 256-channel lab-made pre-amplifier modules (gain settings of 21 dB). The amplified acoustic signals are acquired by four 256-channel DAQ boards (Photosound) with a 20 MHz sampling rate, gain settings of 20 dB and streamed to a workstation by USB 3.0 in real time. A physical picture of the system and its main components are shown in Supplementary Fig. 12. The ultrasound transducer array, motor, pre-amplifiers and DAQs are conveniently installed beneath the bed, allowing the subject to comfortably lie down during system operation. The arc-shaped arrays with a hemispherical housing are positioned below the bed to ensure effective coupling with the imaging targets. Four 256-channel DAQ boards (Photosound) are integrated on the side of the rotational motor. These boards capture and amplify the acoustic signals, enabling further signal processing.

The source ultrasound transducer was positioned at the intersection of the arc-shaped detection arrays, which are mounted on a co-axial stepper motor (NEMA 34, 8V) coupled with a set of two spur gears (Designations, KSS2-20J12 and KSS2-120, gear ratio = 1:6). The stepper motor scans in the azimuthal direction to achieve a 3D panoramic ultrasound detection. The co-axial design of the source ultrasound transducer, arc-shaped detection arrays and the scanning

motor ensures that the virtual point source remains in the same location when the motor scans in the azimuthal direction. In this case, we can assume a consistent acoustic field distribution in the FOV while scanning the ultrasonic arrays for the image reconstruction of 3D RUST. We chose to use a single-element source transducer to reduce the system cost and complexity compared with the use of a large number of pulses and transmission array elements. The arc-shaped detection arrays design with a rotation scanner ensures sufficiently dense elevational and azimuthal sampling to generate a synthetic hemispherical array that offers a panoramic view of the object. With a 20 Hz and 50 Hz PRF, it is equivalent to 800 and 2,000 azimuthal scanning angles to be completed in a 10 s single-breath-hold period, respectively. This is equivalent to having 100 K and 500 K array elements on the hemisphere, respectively.

The FOV can be adjusted by changing the location of the source transducer. We placed the focus of the single-element ultrasonic transducer at the intersection of these arcs to achieve an ~10-cm-diameter FOV. The focus can be adjusted from the axis direction to be above the intersection for reducing FOV or below the intersection to further enlarge the FOV. To synchronize the 3D RUST system, we used a pulse wave signal from the functional signal generator to trigger the DAQ modules, the rotation scanner and the ultrasound source signal generator. The control system was implemented on an Arduino board and a graphical user interface in MATLAB 2019.

The positioning of subjects for head, breast, hand and foot imaging is depicted in Supplementary Fig. 1. For head imaging, subjects assumed a prone position on a height-adjustable bed, and a head support mechanism was used to stabilize the head. A polyvinylidene chloride film was utilized to provide vertical support and restrict head movement, while also preventing cross-contamination between subjects. To achieve optimal acoustic coupling, a small amount of distilled water was applied to the film, and the bowl was filled with D_2O. This configuration minimized light attenuation and ensured effective acoustic coupling between the transducer array and the film. During breast imaging, subjects also assumed a prone position on the bed, with gentle compression of the breast against the polyvinylidene chloride film. Similar to the head imaging set-up, the film provided support, minimized vertical movement of the breast and prevented cross-contamination among subjects. For hand and foot imaging, subjects stood near the system and placed their hand on top of the polyvinylidene chloride film to ensure stability and optimal acoustic coupling. This positioning allowed for accurate imaging while maintaining the necessary stability and contact between the hand and the film surface. Note that the bowl was filled with water for breast, hand and foot imaging.

3D RUS-PAT

The 3D RUST system can be switched to 3D PAT as a hybrid RUS-PAT system by adding laser illumination to the object. We replaced the single source transducer by installing an engineering diffuser (EDC-80, RPC Photonics) sealed in the lens tube at the intersection of the arc-shaped detection arrays. The fluctuation of the light intensity distribution across the angular FOV is within 10% according to the specifications of the diffuser. We utilized 1,064 nm light for illumination with a 20 Hz laser (Litron, PRF, 20 Hz; maximum pulse energy, ~2.5 J). We achieved a similar FOV as RUST of ~10 cm because of the large diverging angle of the engineered diffuser. The FOV can be adjusted by using a diffuser with a different diverging angle. For example, we can use another small diverging engineering diffuser (EDC-50, RPC Photonics) to achieve a 6-cm-diameter FOV. For the current set-up, the radiant exposure (~30 mJ cm^{-2} at 1,064 nm) and fluence rate (~300 mW cm^{-2}) are within the ANSI safety limits[41] (100 mJ cm^{-2} and 1,000 mW cm^{-2} at 1,064 nm). The mechanical index (MI ~ 0.1) and spatial-peak temporal-average intensity (I_{SPTA} ~ 50 mW cm^{-2}) are within the safety limits defined by US Food and Drug Administration's Electronic Product Radiation Control and the International Electrotechnical Commission, which require MI <1.9 and I_{SPTA} <720 mW cm^{-2}. We first performed the 3D PAT scan for 10 s and then switched the system to perform the 3D RUST scan for another 10 s with the subject in the same position.

Image reconstruction

The image reconstruction of 3D RUS-PAT was based on the delay and sum and universal back-projection algorithms[42,43] implemented in MATLAB and C++. In RUST image reconstruction, we collected the ultrasound scattered signals from each array element and scanning position. Then, we reweighted the received signals based on the density of the array elements after scanning. For each voxel in the reconstructed 3D space, we summed the received signal amplitudes with appropriate delays to obtain the reconstructed image. In PAT image reconstruction, we back-projected the received photoacoustic signals at all scanning positions to the 3D space to form a volumetric image. We have also taken into consideration the acceleration and deceleration of the motor at the beginning and end positions during image reconstruction for the coordinates of the synthetic array elements, as illustrated in Supplementary Fig. 13. The voxel size for both modalities is $0.25 \times 0.25 \times 0.25$ mm^3. The reconstructed volumetric images were post-processed using depth compensation and Hessian-based Frangi vesselness filtration.

Imaging protocols

All human imaging experiments were performed with the relevant guidelines and regulations approved by the Institutional Review Board of the California Institute of Technology (Caltech). We have conducted imaging sessions on a total of seven subjects, including one hemicraniectomy patient's head, two subjects' breasts, two subjects' hands and two patients' feet. The human experiments were performed in a dedicated imaging room. Written informed consent was obtained from all the participants according to the study protocols.

Reporting summary

Further information on research design is available in the Nature Portfolio Reporting Summary linked to this article.

Data availability

The data that support the findings of this study are provided within the paper and its Supplementary Information.

Code availability

The algorithms used for photoacoustic and ultrasound image reconstruction are described in detail in Methods. Because a patent application is pending, the corresponding computer codes are not publicly available. Comparable performance can be achieved by following the procedural descriptions provided in this article.

References

1. Schmidt, G., Dinter, D., Reiser, M. F. & Schoenberg, S. O. The uses and limitations of whole-body magnetic resonance imaging. *Dtsch. Arztebl. Int.* **107**, 383–389 (2010).
2. Mazonakis, M. & Damilakis, J. Computed tomography: what and how does it measure? *Eur. J. Radiol.* **85**, 1499–1504 (2016).
3. Edelman, R. R. & Koktzoglou, I. Noncontrast MR angiography: an update. *J. Magn. Reson. Imaging* **49**, 355–373 (2019).
4. Kumamaru, K. K., Hoppel, B. E., Mather, R. T. & Rybicki, F. J. CT angiography: current technology and clinical use. *Radiol. Clin. North Am.* **48**, 213–235 (2010).
5. Szabo, T. L. *Diagnostic Ultrasound Imaging: Inside Out* (Academic Press, 2004).
6. Zhang, Y., Li, H. & Lee, W.-N. Imaging heart dynamics with ultrafast cascaded-wave ultrasound. *IEEE Trans. Ultrason. Ferroelectr. Freq. Control* **66**, 1465–1479 (2019).

7. Zhang, Y. *Functional Ultrafast Ultrasound Imaging of the Cardiovascular System*. PhD Thesis, Univ. Hong Kong (2018).
8. Hatzipanagiotou, M. E. et al. Feasibility of ABUS as an alternative to handheld ultrasound for response control in neoadjuvant breast cancer treatment. *Clin. Breast Cancer* **22**, e142–e146 (2022).
9. Guo, R., Lu, G., Qin, B. & Fei, B. Ultrasound imaging technologies for breast cancer detection and management: a review. *Ultrasound Med. Biol.* **44**, 37–70 (2018).
10. Kratkiewicz, K., Pattyn, A., Alijabbari, N. & Mehrmohammadi, M. Ultrasound and photoacoustic imaging of breast cancer: clinical systems, challenges, and future outlook. *J. Clin. Med.* **11**, 1165 (2022).
11. Kruizinga, P. et al. Compressive 3D ultrasound imaging using a single sensor. *Sci. Adv.* **3**, e1701423 (2017).
12. Christiansen, T. L. et al. 3-D imaging using row–column-addressed arrays with integrated apodization—part II: transducer fabrication and experimental results. *IEEE Trans. Ultrason. Ferroelectr. Freq. Control* **62**, 959–971 (2015).
13. Sauvage, J. et al. 4D functional imaging of the rat brain using a large aperture row-column array. *IEEE Trans. Med. Imaging* **39**, 1884–1893 (2020).
14. Rabut, C. et al. 4D functional ultrasound imaging of whole-brain activity in rodents. *Nat. Methods* **16**, 994–997 (2019).
15. Tanter, M. & Fink, M. Ultrafast imaging in biomedical ultrasound. *IEEE Trans. Ultrason. Ferroelectr. Freq. Control* **61**, 102–119 (2014).
16. Soloukey, S. et al. Functional ultrasound (fUS) during awake brain surgery: the clinical potential of intra-operative functional and vascular brain mapping. *Front. Neurosci.* **13**, 1384 (2020).
17. Demené, C. et al. Transcranial ultrafast ultrasound localization microscopy of brain vasculature in patients. *Nat. Biomed. Eng.* **5**, 219–228 (2021).
18. Yan, J. et al. Transthoracic ultrasound localization microscopy of myocardial vasculature in patients. *Nat. Biomed. Eng.* **8**, 689–700 (2024).
19. Wang, L. V. & Hu, S. Photoacoustic tomography: in vivo imaging from organelles to organs. *Science* **335**, 1458–1462 (2012).
20. Zhang, Y., Olick-Gibson, J., Khadria, A. & Wang, L. V. Photoacoustic vector tomography for deep hemodynamic imaging. *Nat. Biomed. Eng.* **8**, 701–711 (2024).
21. Na, S. et al. Massively parallel functional photoacoustic computed tomography of the human brain. *Nat. Biomed. Eng.* https://doi.org/10.1038/s41551-021-00735-8 (2021).
22. Lin, L. et al. High-speed three-dimensional photoacoustic computed tomography for preclinical research and clinical translation. *Nat. Commun.* **12**, 882 (2021).
23. Kim, J. et al. Programmable real-time clinical photoacoustic and ultrasound imaging system. *Sci. Rep.* **6**, 35137 (2016).
24. Nyayapathi, N. et al. Dual scan mammoscope (DSM)—a new portable photoacoustic breast imaging system with scanning in craniocaudal plane. *IEEE Trans. Biomed. Eng.* **67**, 1321–1327 (2020).
25. Matsumoto, Y. et al. Visualising peripheral arterioles and venules through high-resolution and large-area photoacoustic imaging. *Sci. Rep.* **8**, 14930 (2018).
26. Jeng, G.-S. et al. Real-time interleaved spectroscopic photoacoustic and ultrasound (PAUS) scanning with simultaneous fluence compensation and motion correction. *Nat. Commun.* **12**, 716 (2021).
27. Garcia-Uribe, A. et al. Dual-modality photoacoustic and ultrasound imaging system for noninvasive sentinel lymph node detection in patients with breast cancer. *Sci. Rep.* **5**, 15748 (2015).
28. Coles, J. P. Imaging after brain injury. *Br. J. Anaesth.* **99**, 49–60 (2007).
29. Narayan, R. K. et al. Clinical trials in head injury. *J. Neurotrauma* **19**, 503–557 (2002).
30. Rumboldt, Z., Gordon, L., Bonsall, R. & Ackermann, S. Imaging in head and neck cancer. *Curr. Treat. Options Oncol.* **7**, 23–34 (2006).
31. Tang, Y., Qian, X., Lee, D. J., Zhou, Q. & Yao, J. From light to sound: photoacoustic and ultrasound imaging in fundamental research of Alzheimer's disease. *OBM Neurobiol.* https://doi.org/10.21926/obm.neurobiol.2002056 (2020).
32. Zhang, Y. et al. Transcranial photoacoustic computed tomography of human brain function. Preprint at https://arxiv.org/abs/2206.00248 (2022).
33. Karellas, A. & Vedantham, S. Breast cancer imaging: a perspective for the next decade. *Med. Phys.* **35**, 4878–4897 (2008).
34. Lin, L. et al. Single-breath-hold photoacoustic computed tomography of the breast. *Nat. Commun.* **9**, 2352 (2018).
35. Bevers, T. B. et al. Breast cancer screening and diagnosis. *J. Natl Compr. Cancer Netw.* **7**, 1060–1096 (2009).
36. Garcia, J. & Bianchi, S. Diagnostic imaging of tumors of the hand and wrist. *Eur. Radiol.* **11**, 1470–1482 (2001).
37. Wray, P., Lin, L., Hu, P. & Wang, L. V. Photoacoustic computed tomography of human extremities. *J. Biomed. Opt.* **24**, 026003 (2019).
38. Uhl, A., Busch, C., Marcel, S. & Veldhuis, R. *Handbook of Vascular Biometrics* (Springer Nature, 2020).
39. Wang, Y. et al. A robust and secure palm vessel biometric sensing system based on photoacoustics. *IEEE Sens. J.* **18**, 5993–6000 (2018).
40. Read, J. W. et al. Diagnostic ultrasound of the hand and wrist. *J. Hand Surg.* **21**, 1004–1010 (1996).
41. ANSI Z136.1-2014. American National Standard for Safe Use of Lasers. https://webstore.ansi.org/Standards/LIA/ANSIZ1362014 (2014).
42. Xu, M. & Wang, L. V. Universal back-projection algorithm for photoacoustic computed tomography. *Phys. Rev. E* **71**, 016706 (2005).
43. Li, L. et al. Single-impulse panoramic photoacoustic computed tomography of small-animal whole-body dynamics at high spatiotemporal resolution. *Nat. Biomed. Eng.* **1**, 1–11 (2017).

Acknowledgements

We thank J. Olick-Gibson for proofreading the paper. We thank G. Corral-Leyva for her assistance with the patients. This work was sponsored by the United States National Institutes of Health (NIH) grants R01 CA282505, U01 EB029823 (BRAIN Initiative) and R35 CA220436 (Outstanding Investigator Award).

Author contributions

L.V.W., Y.Z. and S.N. designed the study. Y.Z., L.L., S.N., X.T., J.Z. and K.M. built and modified the system. Y.Z. developed the RUST image reconstruction algorithm. P.H. developed the PAT image reconstruction algorithm. Y.Z., K.S., and S.N. performed the experiments. Y.A. and Y.Z. performed the simulation. Y.Z. and L.V.W. analysed the RUST data. Y.Z., K.S., Y.L. and L.V.W. analysed and interpreted the PAT data. J.J.R. and C.Y.L. recruited the participants and interpreted the head data. T.-W.T., C.Y.L. and J.J.R. recruited the patients with diabetic foot ulcers. Y.Z. wrote the paper with input from all authors. L.V.W. supervised the study and revised the paper.

Competing interests

L.V.W. has a financial interest in Microphotoacoustics, Inc., CalPACT, LLC, and Union Photoacoustic Technologies, Ltd., which, however, did not support this work.

Additional information

Supplementary information The online version contains supplementary material available at https://doi.org/10.1038/s41551-025-01603-5.

Correspondence and requests for materials should be addressed to Charles Y. Liu or Lihong V. Wang.

Peer review information *Nature Biomedical Engineering* thanks the anonymous reviewers for their contribution to the peer review of this work.

nature portfolio

Corresponding author(s): Lihong V. Wang

Last updated by author(s): Sep 5, 2025

Reporting Summary

Nature Portfolio wishes to improve the reproducibility of the work that we publish. This form provides structure for consistency and transparency in reporting. For further information on Nature Portfolio policies, see our Editorial Policies and the Editorial Policy Checklist.

Statistics

For all statistical analyses, confirm that the following items are present in the figure legend, table legend, main text, or Methods section.

n/a	Confirmed	
☐	☒	The exact sample size (*n*) for each experimental group/condition, given as a discrete number and unit of measurement
☐	☒	A statement on whether measurements were taken from distinct samples or whether the same sample was measured repeatedly
☒	☐	The statistical test(s) used AND whether they are one- or two-sided *Only common tests should be described solely by name; describe more complex techniques in the Methods section.*
☒	☐	A description of all covariates tested
☒	☐	A description of any assumptions or corrections, such as tests of normality and adjustment for multiple comparisons
☒	☐	A full description of the statistical parameters including central tendency (e.g. means) or other basic estimates (e.g. regression coefficient) AND variation (e.g. standard deviation) or associated estimates of uncertainty (e.g. confidence intervals)
☒	☐	For null hypothesis testing, the test statistic (e.g. *F*, *t*, *r*) with confidence intervals, effect sizes, degrees of freedom and *P* value noted *Give P values as exact values whenever suitable.*
☒	☐	For Bayesian analysis, information on the choice of priors and Markov chain Monte Carlo settings
☒	☐	For hierarchical and complex designs, identification of the appropriate level for tests and full reporting of outcomes
☒	☐	Estimates of effect sizes (e.g. Cohen's *d*, Pearson's *r*), indicating how they were calculated

Our web collection on statistics for biologists contains articles on many of the points above.

Software and code

Policy information about availability of computer code

Data collection	Matlab 2019a (MathWorks, Inc.). The data collection software is used in licensed technologies, yet they are available from the corresponding authors on reasonable request.
Data analysis	Matlab 2021a (MathWorks, Inc.). The reconstruction codes based on the universal backprojection algorithm are proprietary and used in licensed technologies, yet they are available from the corresponding author on reasonable request.

For manuscripts utilizing custom algorithms or software that are central to the research but not yet described in published literature, software must be made available to editors and reviewers. We strongly encourage code deposition in a community repository (e.g. GitHub). See the Nature Portfolio guidelines for submitting code & software for further information.

Data

Policy information about availability of data

All manuscripts must include a data availability statement. This statement should provide the following information, where applicable:

- Accession codes, unique identifiers, or web links for publicly available datasets
- A description of any restrictions on data availability
- For clinical datasets or third party data, please ensure that the statement adheres to our policy

The data that support the findings of this study are provided within the paper and its supplementary material.

Human research participants

Policy information about studies involving human research participants and Sex and Gender in Research.

Reporting on sex and gender	We imaged two female and five male subjects.
Population characteristics	One hemicraniectomy patient's head, two subjects' breasts, two subjects' hands, and two patients' feet.
Recruitment	Participants were recruited from the California Institute of Technology and the University of Southern California.
Ethics oversight	The study was approved by the Institutional Review Board of the California Institute of Technology.

Note that full information on the approval of the study protocol must also be provided in the manuscript.

Field-specific reporting

Please select the one below that is the best fit for your research. If you are not sure, read the appropriate sections before making your selection.

☒ Life sciences ☐ Behavioural & social sciences ☐ Ecological, evolutionary & environmental sciences

For a reference copy of the document with all sections, see nature.com/documents/nr-reporting-summary-flat.pdf

Life sciences study design

All studies must disclose on these points even when the disclosure is negative.

Sample size	The scope of this work was technology development. We recruited seven subjects.
Data exclusions	No data were excluded from the study.
Replication	The reproducibility of the findings was evaluated via repeated measurements for each subject.
Randomization	Healthy participants were randomly recruited to join the study.
Blinding	The investigators were blinded to group allocation during data collection and analysis.

Reporting for specific materials, systems and methods

We require information from authors about some types of materials, experimental systems and methods used in many studies. Here, indicate whether each material, system or method listed is relevant to your study. If you are not sure if a list item applies to your research, read the appropriate section before selecting a response.

Materials & experimental systems

n/a	Involved in the study
☒	☐ Antibodies
☒	☐ Eukaryotic cell lines
☒	☐ Palaeontology and archaeology
☒	☐ Animals and other organisms
☒	☐ Clinical data
☒	☐ Dual use research of concern

Methods

n/a	Involved in the study
☒	☐ ChIP-seq
☒	☐ Flow cytometry
☒	☐ MRI-based neuroimaging